



Preparation of Polyacrylamide Titanium Dioxide Hybrid Nanocomposite by Direct Polymerization and Its Applicability in Removing Crystal Violet from Aqueous Solution

Dilek Şenol Arslan¹ · Hüseyin Ertap² · Zeynep Mine Şenol³ · Noureddine El Messaoudi⁴ · Valbonë Mehmeti⁵

Accepted: 17 July 2023 / Published online: 2 August 2023

© The Author(s), under exclusive licence to Springer Science+Business Media, LLC, part of Springer Nature 2023

Abstract

The present paper focused on synthesizing a polyacrylamide-titanium dioxide (PAA@TiO₂) nanocomposite using a cross-linking method with N, N'-methylenebisacrylamide and then using this composite to eliminate crystal violet (CV) dye from water and to characterize the adsorbent by XRD, FT-IR, and SEM-EDX techniques. The characterization revealed that TiO₂ nanoparticles dispersed homogeneously within the polymer matrix. The maximum amount of adsorption was about 38.9 mg g⁻¹ under the adsorbent dose of 5 g L⁻¹, 500 mg L⁻¹ CV dye concentration, and pH 6.9. The interaction between the CV molecule and the PAA@TiO₂ nanocomposite surface was studied using Monte Carlo (MC) and molecular dynamics (MD) simulations. The negative value of the Eads (– 586.56 kcal mol⁻¹) of the CV molecules onto the PAA@TiO₂ nanocomposite surface gives credibility to the experimental results. All obtained results showed that PAA@TiO₂ hybrid polymer nanocomposite could be an alternative adsorbent for crystal violet dye removal from wastewater.

Keywords Polyacrylamide · TiO₂ nanoparticles · Nanocomposite · Dye · Adsorption · Wastewater treatment

Introduction

The world's population growth, combined with the continuous and rapid development of industry, causes pollution along with a wide range of other issues such as climate change, desertification, loss of biodiversity, deforestation, destruction of the ozone layer, air, water, and soil pollution,

hazardous and plastic waste, and marine and ocean pollution [1–3]. Industrial wastewater is an essential component of water consumption in the world today. The wastewater from the textile industry [4, 5], which uses large quantities of water in various processes such as dyeing, washing [6], rinsing, and finishing [7], plays a vital role in the environment and health issues [8]. Due to their mutagenic, immunogenic, carcinogenic, and teratogenic characteristics, dyes and heavy metals are considered to be some of the most harmful pollutants in water systems [9, 10]. As a result, finding an effective technique to treat colored wastewater before discharge into bodies of water is essential for human and environmental protection. Researchers and scientists are trying to find solutions to the water pollution problem by developing new alternative materials with excellent adsorbent properties [11, 12].

Titanium dioxide (TiO₂) has been widely researched in recent decades due to its potential scientific and technological applications in a variety of fields, including both synthesis methodologies and broad scientific and technological applications [13, 14] such as biomedical [15], environmental [16], and chemical researches have been discussed by a great number of authors in literature [17]. TiO₂ is well-known for its excellent performance in environmental applications.

✉ Hüseyin Ertap
huseyinertap@kafkas.edu.tr

✉ Zeynep Mine Şenol
msenol@cumhuriyet.edu.tr

¹ Faculty of Engineering, Department of Materials Science & Nanotechnology Engineering, Abdullah Gül University, Kayseri, Turkey

² Faculty of Science and Letters, Department of Physics, Kafkas University, Kars, Turkey

³ Faculty of Health Sciences, Department of Nutrition and Diet, Cumhuriyet University, Sivas, Turkey

⁴ Faculty of Sciences, Laboratory of Applied Chemistry and Environment, Ibn Zohr University, 80000 Agadir, Morocco

⁵ Faculty of Agriculture and Veterinary, University of Prishtina, Prishtina 10000, Kosovo

Because of the large catalyst surface area, TiO₂ dispersed directly into wastewater is effective. It boosts the efficiency of photocatalytic reactions [18, 19]. Its tunable pore size makes it ideal for adsorbing a wide range of molecules [20]. Meanwhile, it has limitations, such as the need to replace the catalyst after treatment. This post-treatment procedure raises capital costs [21].

Recently, conducting polymer-coated TiO₂ nanoparticles [22], heat-treated TiO₂ nanoparticles, Fe-TiO₂ [23], and TiO₂-coated PVDF membranes [24] were prepared for photocatalytic treatment to purify wastewater. TiO₂ can also be modified by incorporating polymer matrices such as polyacrylamide, polyamide, polypropylene, polypyrrole, and polylactic acid [25–27]. As known with literature, PAA is inert hydrogel for CV dye. In studies carried out to date, PAA@TiO₂ nanocomposite has been synthesized by various methods and its adsorbent properties have been investigated. However, as far as we know, no research has been conducted on the usability of this composite in the removal of crystal violet (CV) dye from aqueous solution and its explanation with Monte Carlo and molecular dynamics studies. For this reason, it is thought that this study will make important contributions to the literature. In this paper, the removal of CV dye from water by using the PAA@TiO₂ nanocomposite was studied. The prepared nanocomposite was characterized by several instruments. Batch adsorption experiments were conducted to determine the influence of operational parameters such as initial pH, initial concentration, contact time, temperature, and adsorbent dosage. Then, the CV adsorption ability was examined by analyzing adsorption isotherms, adsorption kinetics, and thermodynamic parameters. Finally, Monte Carlo (MC) and molecular dynamics (MD) simulations are the approaches used to better understand the interaction between CV molecules and the surface PAA@TiO₂ nanocomposite.

Materials and Methods

Reagents and Instrumentation

Reagents: TiO₂ nanoparticles (98% purity) were obtained from Sigma (USA). Acrylamide monomer (AA), ammonium persulphate (APS), N, N' methylene bisacrylamide (MBSA), N, N, N, N-tetramethyl ethylenediamine (TEMED), and crystal violet (C₂₅N₃H₃₀Cl) were obtained from Merck (Germany). KNO₃, HCl, C₂H₅OH, NaOH, and other chemicals were all purchased from Sigma-Aldrich. Double-deionized water was used in all experiments.

Instrumentation: The PAA@TiO₂ nanocomposite and its components were characterized by measurements of scanning electron microscopy (SEM, LEO-EVO 40, Cambridge-Ingiltere), energy-dispersive X-ray spectroscopy (EDX,

Bruker-125 eV, Berlin-Almanya), and Fourier transform infrared spectroscopy (FT-IR, ThermoScientific Nicolet 6700). X-ray diffraction (XRD) was recorded by the Bruker D8Discover. The equilibrium concentrations were measured at λ = 590 nm by obtaining CV dye absorbance utilizing a UV–vis spectrophotometer (UV-DR-6000; Shimadzu, China).

Preparation of PAA@TiO₂ Nanocomposite

A homogeneous combination was created by mixing 1 g of TiO₂ in 20 mL of distilled water and 2 g of AA monomer in 20 mL of distilled water to synthesize about 3 g of PAA@TiO₂ nanocomposite. Then a solution of 0.2 g MBSA for crosslinking was added and stirred. The mixture was then added 200 μL of TEMED and 1 g APS in the rapid cycle at 25 °C. Eventually, the PAA@TiO₂ nanocomposite was obtained. The PAA@TiO₂ nanocomposite dried in the oven at 40 °C was ground and stored in closed containers for later use. The synthesis of the PAA@TiO₂ nanocomposite is presented in Fig. 1.

Batch Adsorption

The CV dye adsorption onto the PAA@TiO₂ nanocomposite was tested in batch method. The batch experimental was carried out in a series of test tubes containing 10 mL of dye solution in contact with 50 mg of adsorbent at 25 °C for 24 h. These were allowed to reach equilibrium, and then CV dye equilibrium concentrations were determined using a UV–vis spectrophotometer at λ = 590 nm. Hence, the PAA@TiO₂ adsorption capacity Q (mg g⁻¹) and the rate of CV dye uptake (Removal %) were estimated using Eqs. 1 and 2, respectively [28]:

$$Q = \left[\frac{C_i - C_f}{m} \right] x V \quad (1)$$

$$\text{Removal \%} = \left[\frac{C_i - C_f}{C_i} \right] \times 100 \quad (2)$$

C_i is preliminary and C_f is the equilibrium conc. (mg L⁻¹) of CV, V is the volume of CV dye solution (L), and m is the mass of adsorbent (g) [29].

Computational Details

The size of the models employed in the calculations was constructed using the Biovia software [30, 31]. The model surface was constructed by packing 10 chains of (10 monomeric units) + two TiO₂ clusters and structurally optimizing the periodic boundary condition (PBC) cell geometry as

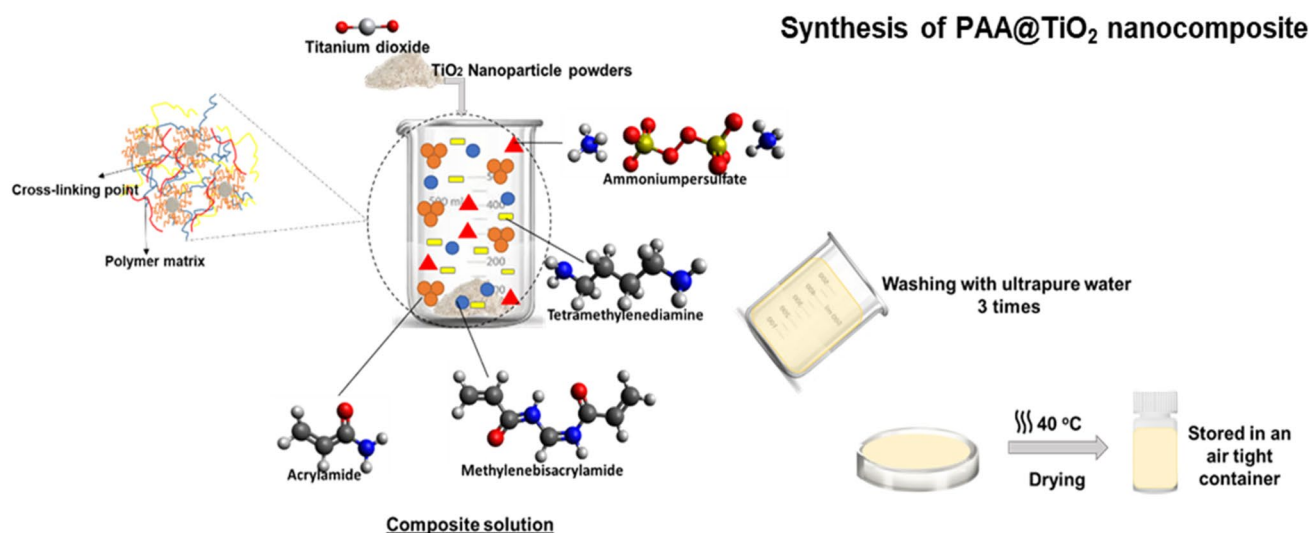


Fig. 1 The schematic representation of the synthesized PAA@TiO₂ nanocomposite

presented in Fig. 2a. The PAA chains prior to their packing were undergone a conformer search (Random sampling method, Compass III forcefield, number of conformers 1000) in order to start from the lowest energy structures (Fig. 2b) [32].

The PBC surface was further combined with a 45 Å vacuum layer [to accommodate CV molecules and solvent: 500 water molecules] [33–35]. The Compass III forcefield was used for the MC simulations and molecular dynamic (MD) calculations [36, 37]. MD simulations in the forcite module of Material Studio at a temperature of 295 Kelvin (using the Berendsen thermostat). The duration of the simulation was 800 picoseconds. Using the trajectory of the MD simulation, a radial distribution function (RDF) was generated. This was performed so that a forecast could be made about how the inhibitor molecule adsorbs [38, 39].

Results and Discussion

XRD Analysis

The XRD spectra of PAA, TiO₂ nanoparticles and PAA@TiO₂ nanocomposite are given in Fig. 3. The XRD spectrum of PAA showed that PAA is amorphous structure. All the XRD diffraction peaks of TiO₂ nanoparticles and PAA@TiO₂ nanocomposite were observed in the patterns of anatase-type titanium (JCPDS Card No: 21-1272). The XRD spectrum of the PAA@TiO₂ nanocomposite showed that the anatase-type structure of the TiO₂ nanoparticles was preserved. The strongest diffraction peaks observed around $2\theta = 25.355^\circ$, and $2\theta = 25.337^\circ$ in the XRD patterns correspond to diffraction from the (101) plane for TiO₂ nanoparticles and PAA@TiO₂ nanocomposite,

respectively. The diffraction peaks appeared around $2\theta = 25.355^\circ$, 37.859° , 47.960° , 54.470° , and 62.581° for TiO₂ nanoparticles and $2\theta = 25.337^\circ$, 37.801° , 47.931° , 54.430° , and 62.493° for PAA@TiO₂ nanocomposite, respectively. XRD patterns showed that the peaks are due to diffraction from the (101), (004), (200), (105), and (204) planes of both TiO₂ nanoparticles and PAA@TiO₂ nanocomposite, respectively. The XRD patterns given in Fig. 3 are in good agreement with the literature [40–42]. The peak positions of PAA@TiO₂ nanocomposite shifted to smaller degrees compared to the peak positions of TiO₂ nanoparticles. Similar situations were observed at Full Width Half Maximum (FWHM) values of TiO₂ nanoparticles and PAA@TiO₂ nanocomposite. The crystallite size (*D*) is calculated from the XRD data using Scherrer equation [43]:

$$D = \frac{K\lambda}{\beta \cos \theta} \quad (3)$$

where λ is the wavelength (0.15418 nm) of the Cu K_α radiation, *K* is the Scherrer constant taken as 0.94, θ is the Bragg angle of the diffraction peak considered and β is the FWHM of the diffraction peak. The crystallite size (*D*) and residual strain (ϵ) were calculated for four diffraction peaks of TiO₂ nanoparticles and PAA@TiO₂ nanocomposite by using equations in the literature [43] and the results are presented in Table 1. It is seen clearly that the crystallite size (*D*) values of PAA@TiO₂ nanocomposite are greater than TiO₂ nanoparticles but, the residual strain (ϵ) values of PAA@TiO₂ nanocomposite are smaller than TiO₂ nanoparticles.

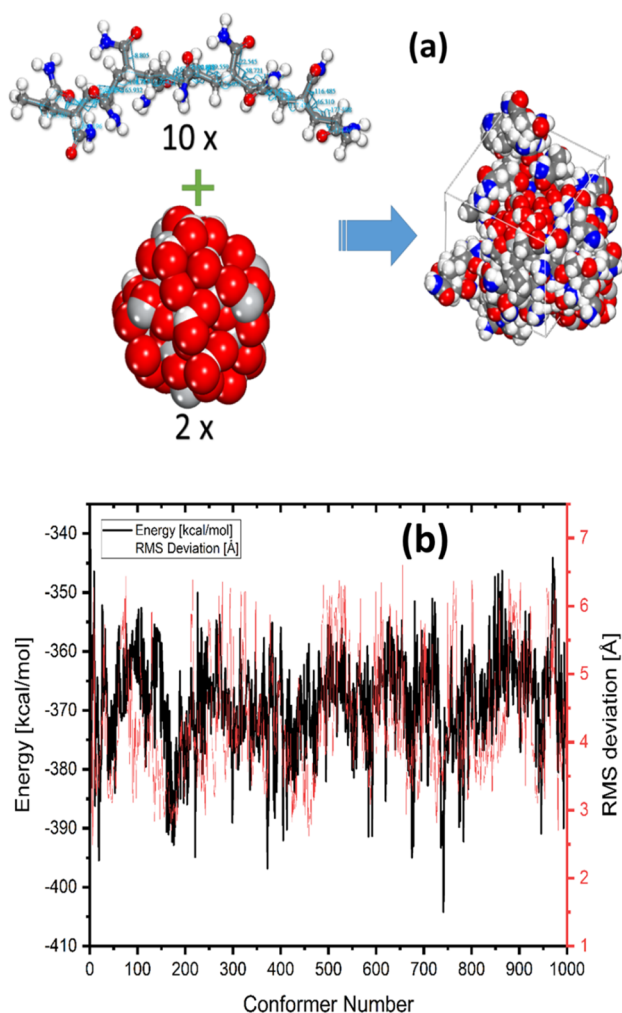


Fig. 2 Construction of PCB cell to model the PAA@TiO₂ nanocomposite surface (a) and generated number of conformers and their corresponding energies (b)

FT-IR Analysis

Figure 4 shows the FT-IR spectra of PAA, TiO₂ nanoparticles, and the PAA@TiO₂ nanocomposite. On the FT-IR spectrum of TiO₂ nanoparticles, the peak at 3254 cm⁻¹ represents -OH groups. The peak at 1639 cm⁻¹ and the peak at 427 cm⁻¹ are Ti-O-Ti tensile vibrations. Ti-O peaks are observed at 633 cm⁻¹ and 511 cm⁻¹ [44, 45]. On the FT-IR spectrum of PAA, hydroxyl (-OH) groups band on the surface at 3338 cm⁻¹ [46, 47], N-H vibrations peak at 3185 cm⁻¹, CH₂ stretching vibrations at 2934 cm⁻¹, peaks at 1646 cm⁻¹ and 1608 cm⁻¹ represents C=O groups [48]. It represents the peak C-N vibrations at 1450 cm⁻¹, the peak C-H vibrations at 1318 cm⁻¹ and the peak NH₂ stretching vibrations at 1113 cm⁻¹. On the FT-IR spectrum of PAA@TiO₂ nanocomposite, a characteristic peak of surface -OH groups was observed at 3323 cm⁻¹. N-H

vibrations were observed at 3185 cm⁻¹, CH₂ at 2934 cm⁻¹, C=O at 1636 cm⁻¹ and 1449 cm⁻¹, and C-N vibrations at 1449 cm⁻¹. Ti-O and Ti-O-Ti peaks were observed at 778 cm⁻¹ and at 458 cm⁻¹, respectively. The presence of both PAA and TiO₂ peaks in the FT-IR spectra of PAA@TiO₂ confirmed PAA@TiO₂ synthesis.

Figure 5 shows the comparison of the FT-IR spectra before and after the adsorption of CV dye on PAA@TiO₂ nanocomposite. When Fig. 5 is examined, four new peak formations of CV dye are seen after adsorption. For CV dye, O-H stretches of hydroxyl groups, phenols and water molecules at 3474 cm⁻¹, C-H stretches of CH₃ groups at 2985 cm⁻¹, C-N stretches of aromatic tertiary amine groups at 1355 cm⁻¹, and C-N stretching vibrations of tertiary amine groups at 1170 cm⁻¹ are characteristic peaks [49]. The other peak intensities that increased and decreased after adsorption was considered to be proof of CV dye adsorption.

SEM-EDX Analysis

The visualization of sample surface morphologies of TiO₂ nanoparticles, PAA@TiO₂, and CV adsorbed PAA@TiO₂ nanocomposite has been realized using SEM-EDX analysis, as depicted in Fig. 6. As seen in Fig. 6a, TiO₂ nanoparticles have an ellipsoid, spherical, and uniform size distribution structure [50, 51]. The EDX mapping image and EDX spectrum of TiO₂ showed that TiO₂ contained the elements Ti and O (Figs. 6d and g). The absence of other elements other than Ti and O in the EDX analysis results of TiO₂ nanoparticles confirms the purity of the nanoparticles.

SEM image of the PAA@TiO₂ nanocomposite (Fig. 6b) shows that TiO₂ is covered by PAA. It can be clearly seen that the surface morphology of the PAA@TiO₂ nanocomposite is quite different from that of TiO₂ nanoparticles, N and C elements were also seen along with Ti and O (Fig. 6e). The composite formation of TiO₂ nanoparticles with PAA hydrogel was confirmed by the detection of C, O, N, and Ti elements in PAA@TiO₂ nanoparticles (Figs. 6e and h).

It is evident from the surface smoothing that after adsorption, CV dye molecules aggregate on the surface of the PAA@TiO₂ nanocomposite (Fig. 6c). The EDX mapping image and EDX spectrum of the CV-loaded PAA@TiO₂ nanocomposite showed that the CV-loaded nanocomposite included C, O, N, Ti, and Cl (Figs. 6f and i). The presence of Cl atoms in the structure of the CV dye after adsorption was evaluated as evidence for adsorption.

Effect of pH

The influence of pH on the quantity adsorbed of CV was studied by putting in contact with a mass of 50 mg of the PAA@TiO₂ nanocomposite with 10 mL of the dye of a concentration of 500 mg L⁻¹ and varying the pH between

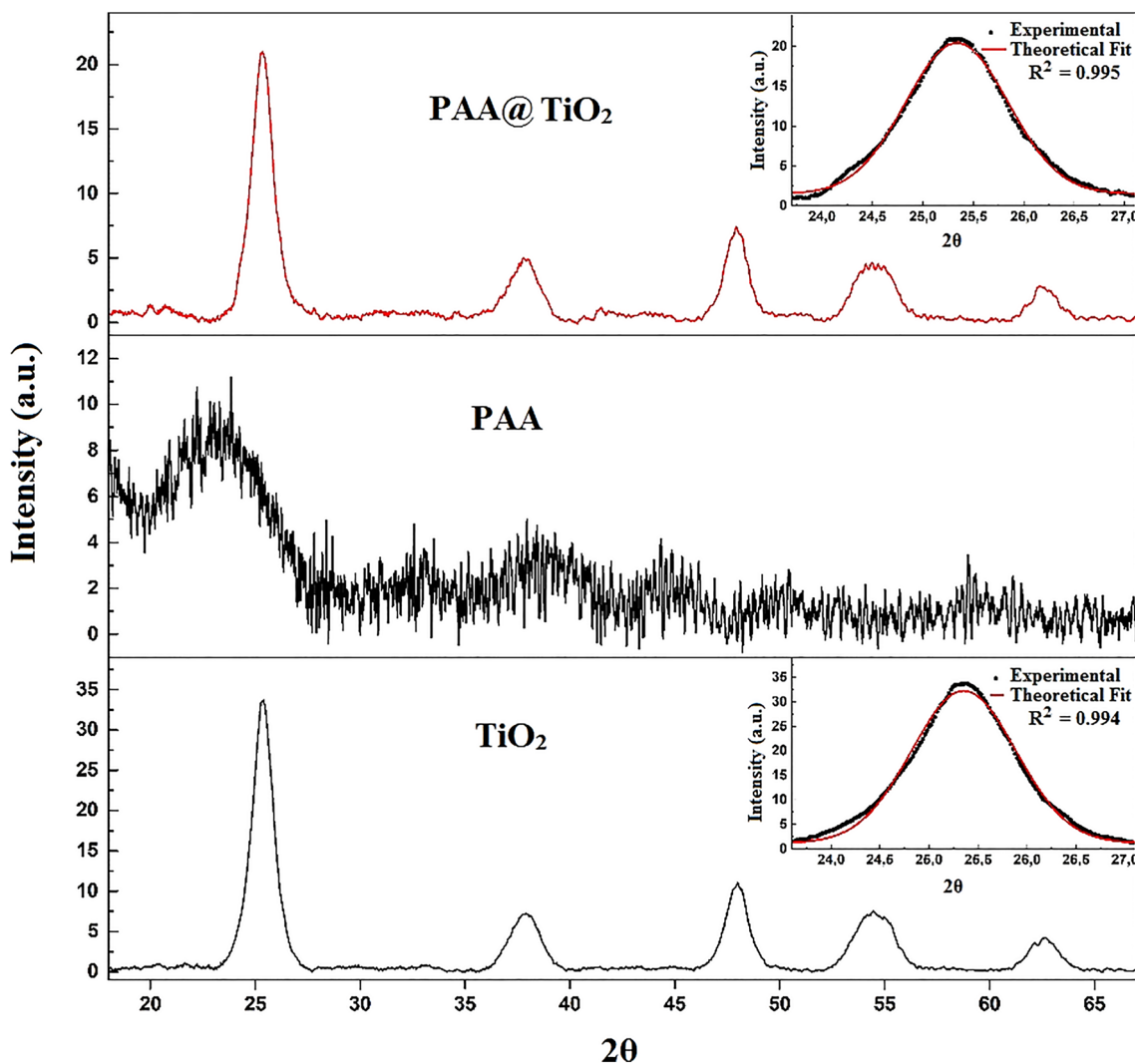


Fig. 3 XRD spectra of TiO₂ nanoparticles and PAA@TiO₂ nanocomposite

Table 1 The FWHM (β), the crystallite size (D), and residual strain (ϵ) values for TiO₂ nanoparticles and PAA@TiO₂ nanocomposite

Sample	Peak	2 θ	FWHM (β)	$\beta \cdot \cos\theta$	D(nm)	ϵ (lin ⁻² . m ⁻⁴) × 10 ⁻⁴
TiO ₂	(1 0 1)	25.355	1.2525	0.0220	6.584	54.984
PAA@TiO ₂		25.337	1.1956	0.0210	6.897	52.489
TiO ₂	(0 0 4)	37.859	1.7348	0.0307	4.718	76.739
PAA@TiO ₂		37.801	1.6883	0.0299	4.848	74.681
TiO ₂	(2 0 0)	47.960	1.2492	0.0223	6.497	55.723
PAA@TiO ₂		47.931	1.2294	0.0219	6.602	54.838
TiO ₂	(2 0 4)	62.581	1.6586	0.0300	4.817	75.153
PAA@TiO ₂		62.493	1.4886	0.0270	5.368	67.442

2 and 12 by the addition of hydrochloric acid (0.1 mol L⁻¹) or sodium hydroxide (0.1 mol L⁻¹) with the help of a pH-meter. The variations in the quantity adsorbed of CV according to the pH are presented in Fig. 7. The

determination of the adsorbent’s point of zero charges (pH_{pzc}) can support the understanding of the sorption mechanism [52]. The pH_{pzc} of the nanocomposite was assessed by means of the pH drift technique [53]. At pH

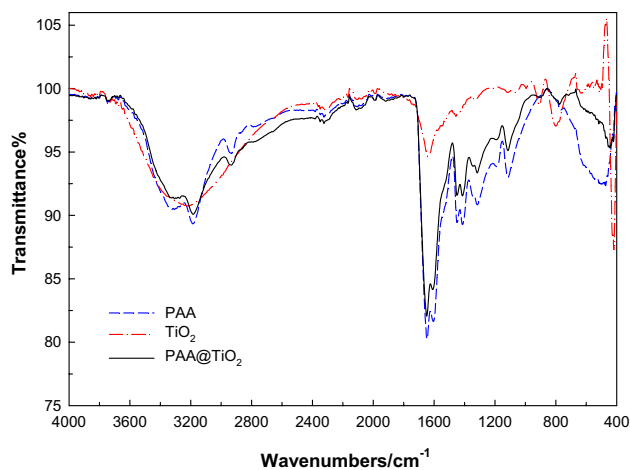


Fig. 4 FT-IR spectra of PAA, TiO₂, and PAA@TiO₂ nanocomposite

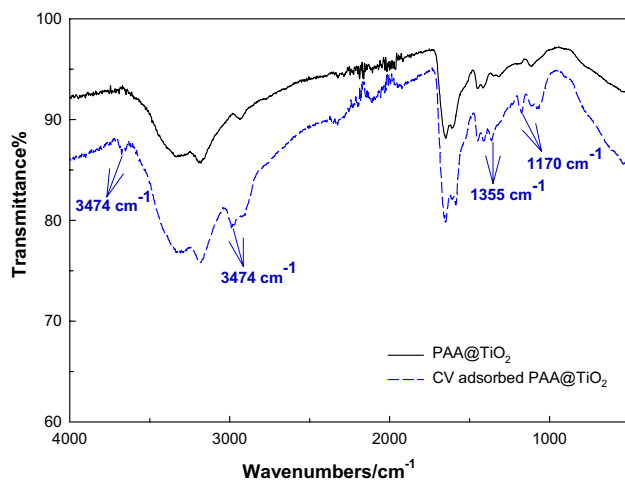


Fig. 5 FT-IR spectra of PAA@TiO₂ and CV adsorbed PAA@TiO₂ nanocomposite

values greater than pH_{PZC} , the sorbent surface bears a negative charge, supporting the sorption of positive ions, and at pH values lower than pH_{PZC} , the surface bears a positive charge, adsorbing negative ions [54]. The pH_{pzc} of the PAA@TiO₂ nanocomposite was 4.47. It is clear that the adsorption of CV by the PAA@TiO₂ nanocomposite took place when the solution $\text{pH} > \text{pH}_{\text{pzc}}$, this means that the surface of the substrates is negatively charged at this point, which favors the adsorption of CV on the PAA@TiO₂, which leads to an increase in the quantity of CV adsorbed with the increase in pH, as explained in Fig. 7 and the obtained results also show that the quantity adsorbed of CV increases from 27.67 to 29.95 mg g^{-1} when the pH goes from 2 to 12. This increase may be attributed to the presence of an electrostatic attraction between the

negative sites on the surface of PAA@TiO₂ and positively charged molecules of the dye [55]. On the other hand, for $\text{pH} < \text{pH}_{\text{pzc}}$, the surface of PAA@TiO₂ nanocomposite is positively charged which leads to repulsion between the cations of the dye and the surface of the adsorbent [56].

Effect of Adsorbent Dosage

The influence of the PAA@TiO₂ dosage on CV adsorption was determined; the doses were in the range of 1 to 20 g L^{-1} , keeping the other parameters constant: [CV]: 500 mg L^{-1} , temperature: 25 °C and pH: 6.9. The results obtained are presented in Fig. 8. The figure shows that the adsorption rate increases from 5.24 to 55.90% with the increase of the PAA@TiO₂ dosage from 1 to 20 g L^{-1} , while the quantity adsorbed decreases from 35.47 to 8.63 mg g^{-1} . This phenomenon could be explained by the fact that an increase in the dose leads to an increase in the exchange surface, specifically the availability of the adsorption sites [57].

Adsorption Isotherm Models

Experimental data for CV adsorption onto PAA@TiO₂ nanocomposite were obtained at 25 °C, with the CV concentration in the range of 10–1000 mg L^{-1} concentration. Three isotherm models namely Langmuir (Eq. 4), Freundlich (Eq. 5), and Dubinin-Radushkevich (D-R) (Eqs. 6–8) were employed to fit the experimental data, and parameters are presented in Table 2.

$$Q_e = \frac{Q_m C_e}{1 + K_L C_e} \quad (4)$$

$$Q_e = X_F C_e^\beta \quad (5)$$

$$Q_e = X_{DR} e^{-(K_{DR} \epsilon^2)} \quad (6)$$

$$\epsilon = RT \ln \left(1 + \frac{1}{C_d} \right) \quad (7)$$

$$E_{DR} = (2K_{DR})^{-0.5} \quad (8)$$

The fit of the experimental data to the isotherms is presented in Fig. 9. Comparing the fit with the Langmuir, Freundlich, and D-R isotherm models, it is seen that the Langmuir model fits the experimental data with a higher correlation coefficient (R^2 : 0.982). The fact that the adsorption energy value found from the D-R isotherm

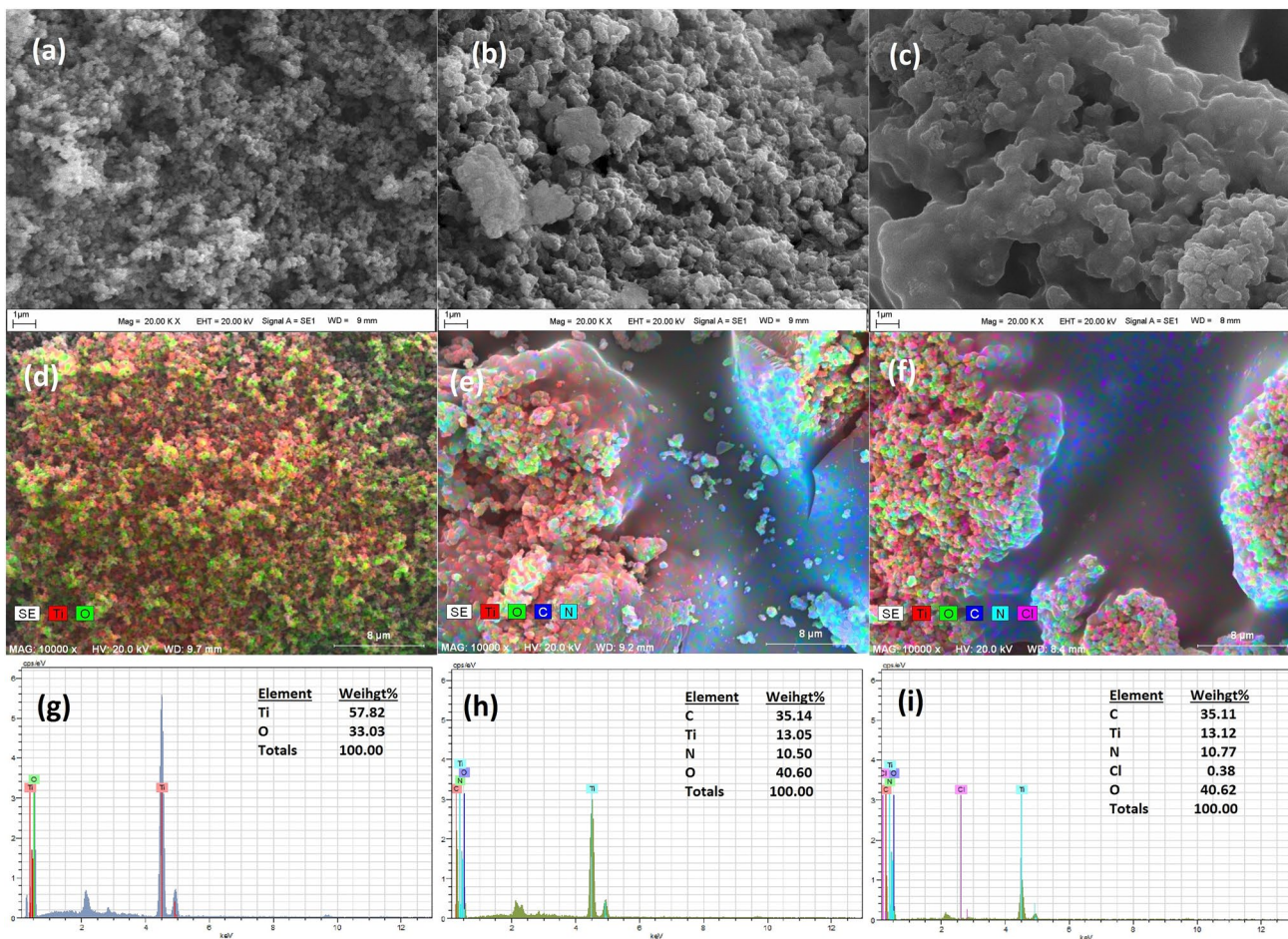


Fig. 6 SEM surface morphologies of TiO₂ nanoparticles (a), PAA@TiO₂ (b), and CV adsorbed PAA@TiO₂ (c), and their corresponding EDX mapping images (d–f) and EDX spectra (g–i), respectively

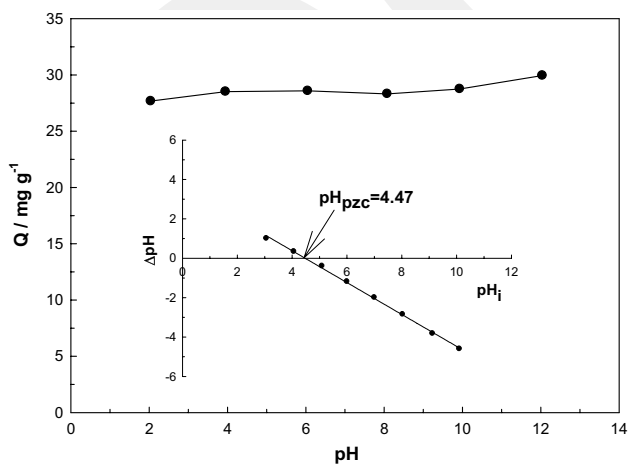


Fig. 7 Effect of pH on the CV adsorption

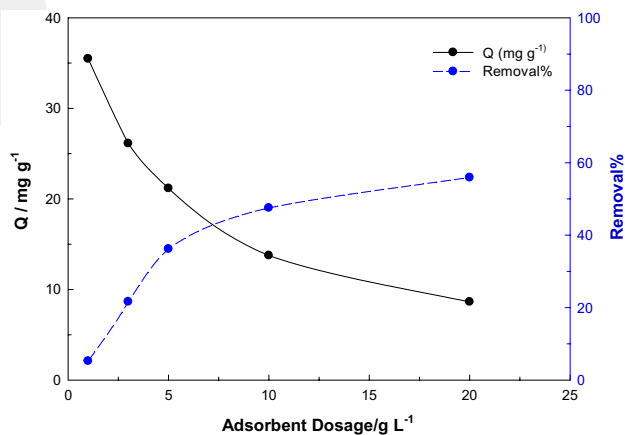
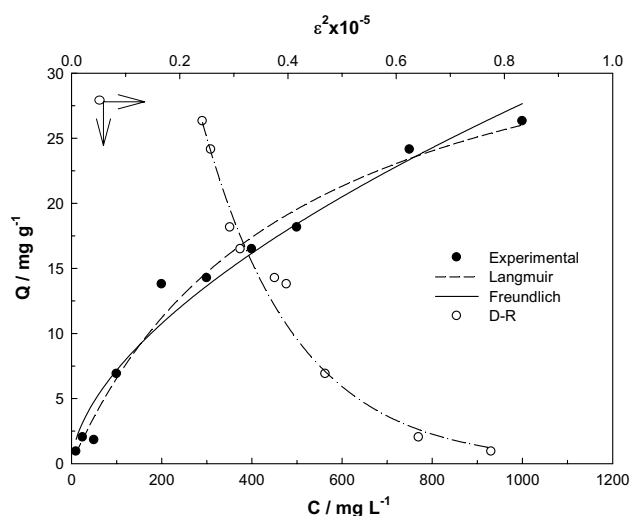


Fig. 8 Effect of PAA@TiO₂ dosage on CV adsorption

Table 2 Isotherm's parameters were calculated from Langmuir, Freundlich, and D-R isotherm models

Isotherm model	Parameter	Value
Langmuir	Q_m (mg g ⁻¹)	38.9
	K_L (L mg ⁻¹)	0.0078
	R^2	0.982
Freundlich	X_F	0.482
	B	0.586
	R^2	0.970
D-R	X_{DR} (mg g ⁻¹)	106
	$-K_{DR} \times 10^9$ (mol ² kJ ⁻²)	5.78
	E_{DR} (kJ mol ⁻¹)	9.31
	R^2	0.962

**Fig. 9** Adsorption isotherms for CV

was 9.31 kJ mol⁻¹ ($E > 8$ kJ mol⁻¹) also showed that the adsorption process was chemical [58].

Table 3 Comparison of sorption capacities of other adsorbents for CV dye removal

Adsorbent type	pH	T (°C)	Q_{max} (mg g ⁻¹)	References
NaOH-modified rice husk	8	20	44.87	[59]
Kaolin	7	22	47.27	[60]
Modified Bambusa Tulda	7	25	20.84	[61]
Magnetic activated carbon	9.5	25	12.59	[62]
Iron-manganese oxide-coated kaolinite	7	35	20.64	[63]
Polymer nanocomposite	–	50	20.92	[64]
Chitin nanowhiskers	–	25	39.56	[65]
Coniferous pinus bark	–	30	32.78	[66]
κ -carrageenan-g-poly(methacrylic acid)	7	–	28.24	[67]
Nanomagnetic iron oxide	7	–	16.50	[68]
PAA@TiO ₂ nanocomposite	6.9	25	38.90	This study

The PAA@TiO₂ nanocomposite exhibited a relatively higher adsorption capacity than many adsorbents in the literature (Table 3). Therefore, PAA@TiO₂ can be considered a promising adsorbent to remove CV from the aqueous medium.

Adsorption Kinetics

It is very important to determine the time that the adsorption process reaches equilibrium to define the effectiveness of the adsorbent in controlling water pollution. Figure 10a was examined, and it was seen that the adsorption capacity increased by 23.90 mg g⁻¹ in 360 min. It reached the equilibrium concentration of 25.41 mg g⁻¹ in approximately 420 min. The high rate of adsorption in the initial stage of adsorption is due to the abundance of active centers on the nanocomposite surface [69]. Then, with the decrease in active centers on the nanocomposite surface, the rate of adsorption slowed down. The abundance of functional groups on the nanocomposite surface, and active adsorption sites accelerated intraparticle diffusion [70], resulting in rapid adsorption. Rapid adsorption is one of the desirable properties for both small-scale and large-scale applications.

Pseudo-first-order (PFO) [71], pseudo-second-order (PSO) [72], and intraparticle diffusion (IPD) [73] kinetic models were preferred for the evaluation of adsorption of CV on PAA@TiO₂ nanocomposite (Fig. 10; Table 4). The linear (Eq. 9–10) and non-linear (Eq. 11–12) the PFO, and PSO kinetic models equation rate expressions are given below [74]. The IPD are given in Eq. 13.

$$\log(Q_e - Q_t) = \log Q_e - k_1 t \quad (9)$$

$$\frac{t}{Q_t} = \frac{1}{k_2 Q_e^2} + \frac{t}{Q_e} \quad (10)$$

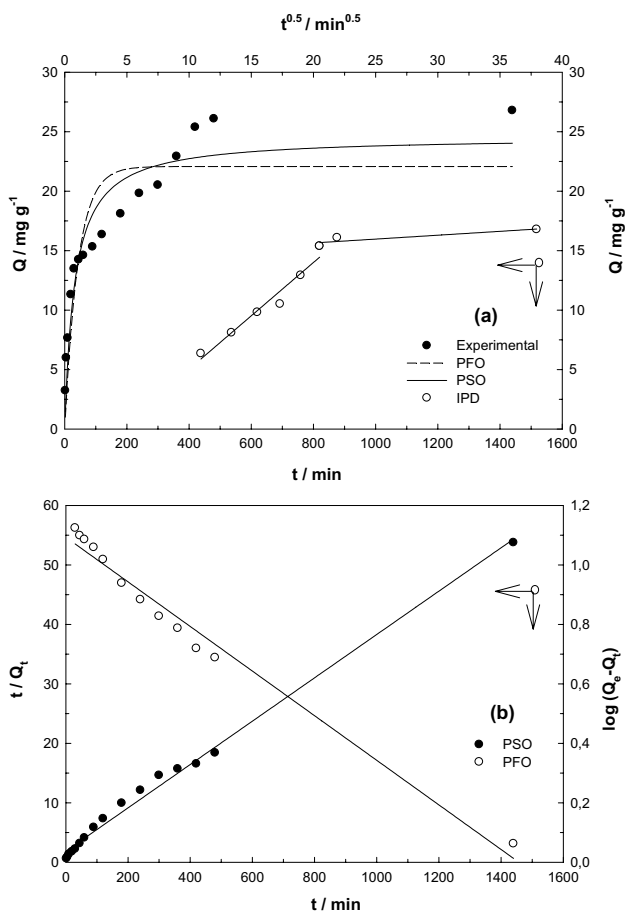


Fig. 10 Non-linear (a) and linear (b) adsorption kinetics

$$Q_t = Q_e(1 - e^{-k_1t}) \tag{11}$$

$$Q_t = \frac{Q_e^2 k_1 t}{Q_e k_2 t + 1} \tag{12}$$

$$Q_t = k_1 t^{0.5} \tag{13}$$

The correlation coefficient values of the PSO non-linear ($R^2:0.900$) and linear ($R^2:0.993$) were found to be greater than the regression coefficient values of the PFO non-linear ($R^2:0.799$) and linear ($R^2:0.979$). As shown in Table 4, the calculated value of non-linear Q_t (24.6 mg g^{-1}) and linear Q_t (27.4 mg g^{-1}) from the PSO model was very close to the experimental value of Q_e (26.1 mg g^{-1}), which indicates that this model is also suitable for describing the adsorption process on the surface of the PAA@TiO₂. It means that there are no significant differences between non-linear and linear kinetic models and that the PSO model is the better option [75].

When the CV dye adsorption kinetics on the PAA@TiO₂ nanocomposite are examined, it is seen that the adsorption takes place rapidly up to the first 120 min (Fig. 10a). Afterward, it is seen that adsorption increases relatively slowly with contact time. When 240 min has reached, the adsorption has now reached equilibrium since all adsorptive areas are filled with CV dye molecules. When the IPD model graphs (Fig. 10a) are examined, two linear parts that do not pass through the origin are seen. The first part represents the diffusion process into the boundary layer. The second part refers to the adsorption to the pores of the adsorbent. When all these results are evaluated together, it is understood that it is not possible to explain the adsorption kinetics with a single mechanism.

Adsorption Thermodynamics

Thermodynamic studies play a pivotal role in determining the nature of the adsorption process. The following equations can be used to calculate the thermodynamic parameters in accordance with the laws of thermodynamics:

$$\Delta G^\circ = -RT \ln K_D \tag{14}$$

$$K_D = \frac{Q_e}{C_e} \tag{15}$$

Table 4 The calculated parameters from kinetic models

Kinetic model	Parameter	Value (Non-linear)	Value (Linear)
PFO	Q_t (mg g ⁻¹)	22.11	12.4
	Q_e (mg g ⁻¹)	26.1	26.1
	$k_1 \times 10^3$ (min ⁻¹)	23.20	75
	R^2	0.799	0.979
PSO	Q_t (mg g ⁻¹)	24.6	27.4
	Q_e (mg g ⁻¹)	26.1	26.1
	$k_2 \times 10^3$ (mg ⁻¹ g min ⁻¹)	1.26	71.5
	R^2	0.900	0.993
IPD	$k_1 \times 10^3$ (mg g ⁻¹ min ^{-0.5})	14,340	
	R^2	0.803	

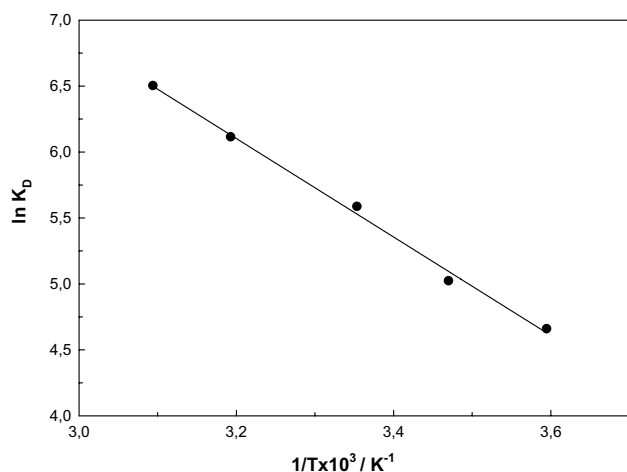


Fig. 11 The effect of temperature on the adsorption

Table 5 Thermodynamic parameters for CV dye removal

Temperature (°C)	ΔG° (kJ mol ⁻¹)	ΔH° (kJ mol ⁻¹)	ΔS° (J mol ⁻¹ K ⁻¹)
5	-10.9	31.1	151
15	-12.5		
25	-14.0		
40	-16.3		
50	-17.8		

$$\ln K_D = \frac{\Delta S^\circ}{R} - \frac{\Delta H^\circ}{RT} \quad (16)$$

where K_D symbolizes the adsorption equilibrium constant, and. Plotting $\ln K_D$ as a function of $1/T$ (Fig. 11) yields a straight line with a slope $-\Delta H^\circ/R$ and $\Delta S^\circ/R$ intercept at different temperatures, including 5 °C, 15 °C, 25 °C, 40 °C and 50 °C. The results obtained are grouped together in Table 5. As seen in Table 5, adsorption enthalpy (ΔH°) change was positive in CV dye adsorption to PAA@TiO₂ nanocomposite. The adsorption of CV dye onto PAA@TiO₂ nanocomposite was an endothermic process, as evidenced by the positive enthalpy (ΔH°) [76]. Gibbs free energy ΔG° values were negative and increased with increasing temperatures, indicating that the adsorption of CV dye on PAA@TiO₂ [77, 78]. The positive entropy (ΔS°) value indicates that the irregularity of the PAA@TiO₂ nanocomposite-CV dye solution interface has increased and the affinity of the PAA@TiO₂ nanocomposite to the CV dye has increased [79].

MC and MD Calculations

Calculating energy outputs requires determining the best adsorption arrangement of adsorbate molecules on the adsorbent's surface. This method computes adsorption energy based on adsorbate-adsorbent interactions. We're using the equation below to calculate adsorption energy (E_{ads}) [80–82]:

$$E_{ads} = E_{PAA@TiO_2Surface/CV} - (E_{PAA@TiO_2Surface} + E_{CV}) \quad (17)$$

where $E_{PAA@TiO_2 surface/CV}$ is the total energy of the simulated adsorption system, $E_{PAA@TiO_2 surface/CV}$ and E_{CV} are the total energies of the CV molecules and nanocomposite adsorbent, respectively.

MC computations are used to simulate the adsorption of the CV molecule onto the modeled PAA@TiO₂ nanocomposite surface. This technique of calculating molecular complexity uses random permutations of simulation box species (molecules, ions) [83]. The energy development of the most favorable or low-energy adsorption sites near the adsorbent surface is depicted in Fig. 12, as calculated by MC simulations.

A significantly larger negative value of E_{ads} of the adsorbate molecules onto the adsorbent surface gives credibility to the experimental results. The analysis of the MC final geometrical position supports this inference by showing that the CV is located quite near the surface [32, 84].

It is often believed that MD is a more accurate method of demonstrating the dynamics of adsorption [85, 86]. The interaction may also be easily visualized by evaluating the adsorption geometries with the lowest energy, which can

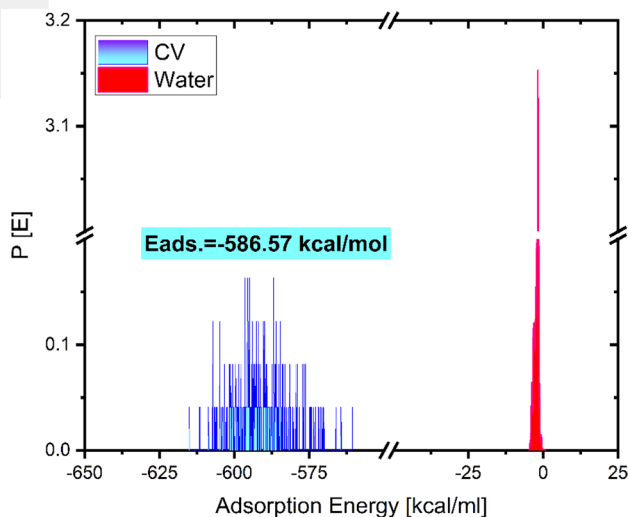


Fig. 12 Probability of the adsorption energy distributions during MC for the CV molecules on the modeled PAA@TiO₂ nanocomposite surface

Fig. 13 Lowest energy poses obtained after MC and MD for the CV molecule on the modeled PAA@TiO₂ nanocomposite surface

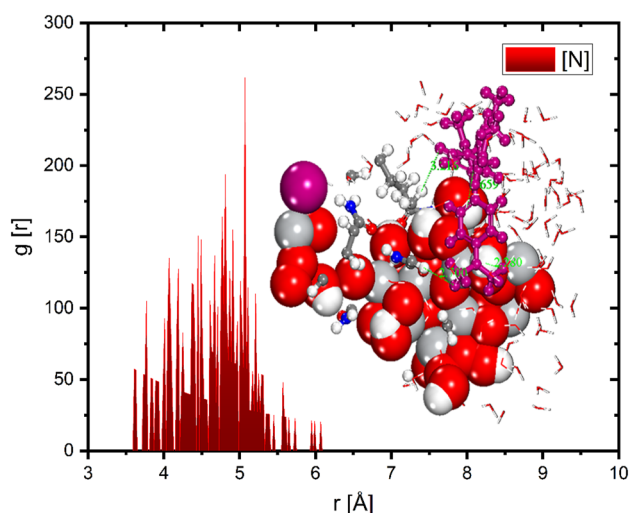
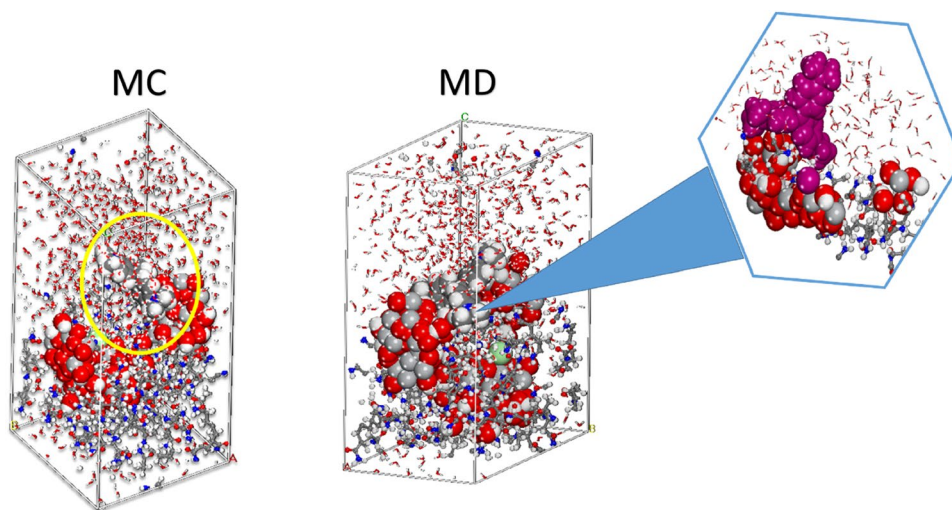


Fig. 14 RDF graph and lowest energy adsorption pose inset as obtained at the end of MD simulation

be acquired from either MC or MD simulations. As can be seen in Fig. 13, the CV molecule is adsorbing itself close to the interface that is composed of polyacrylamide and TiO₂ nanoparticles in both of the scenarios.

RDF analysis, which is performed on the MD trajectory data gathered during adsorption simulations, is a straightforward and uncomplicated method for exploring the adsorption of molecules on surfaces [87]. When the peak is between 1 and 3.5 Å, chemisorption is probable at work. For physisorption, the RDF peaks are predictable to appear at distances greater than 3.5 Å. RDF peak values (Fig. 14) amid the O atom (from TiO₂) and the N atom from the CV are found at larger distances than 3.5 Å [88]. In this case, it seems that the CV is at the limit between physisorption and chemisorption. Due to the flexibility of the polymer and the maneuverability of adsorption, the RDF calculation in

this case is only semi-quantitative. This conclusion is drawn from the closeness of the CV to the interface, as shown in the inset image of Fig. 14.

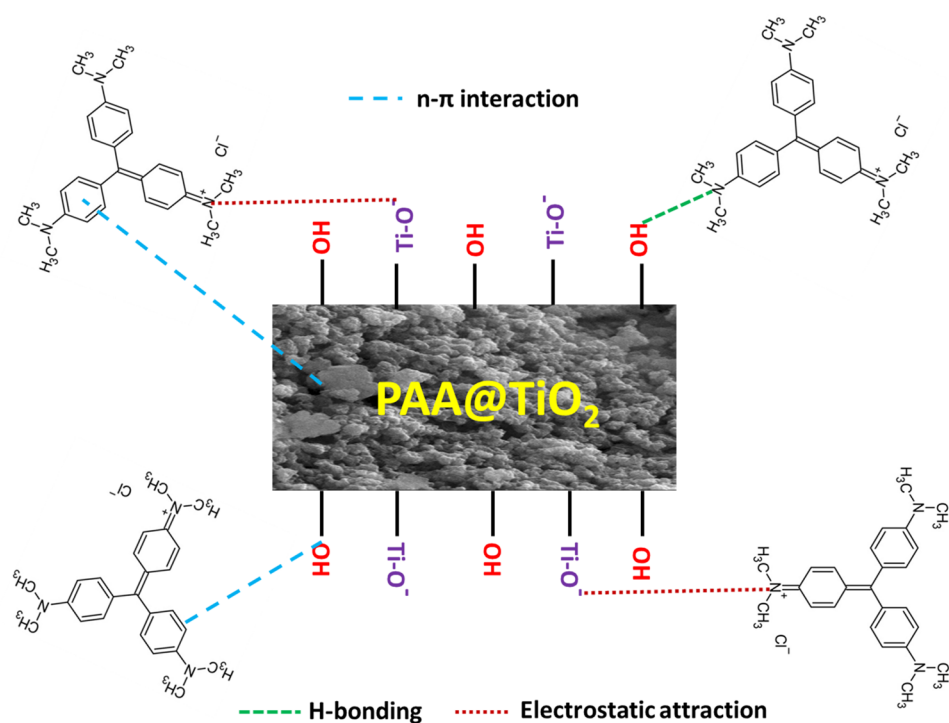
Proposed Adsorption Mechanism

According to the obtained results and based on the CV dye structure and surface properties of the PAA@TiO₂ nanocomposite, it can be assumed that the adsorption mechanism involves the following steps: The CV dye adsorbs in two steps: first, it migrates from the bulk solution to the surface, and second, it diffuses through the boundary layer to the pores of the PAA@TiO₂ nanocomposite. Electrostatic attraction plays an important role in the adsorption process, and hydrogen bonding and n- π interaction also contribute, as displayed in Fig. 15.

Conclusions

This work describes the use of PAA@TiO₂ nanocomposite as an efficient and inexpensive adsorbent to remove CV dye from water. The maximum CV dye removal rate of the PAA@TiO₂ nanocomposite was reached at natural pH:6.9, 25 °C, and 24 h. The maximum adsorption capacity was found to be 38.9 mg g⁻¹. According to the adsorption isotherms of the study, it was found that the AR dye adsorption to the PAA@TiO₂ nanocomposite adsorbent was monolayer on a homogeneous and chemisorption because the binding energy for both dye was more than 8 kJ mol⁻¹. The thermodynamic analysis, which confirms that the reaction was endothermic and spontaneous. The theoretical simulations (Monte Carlo and molecular dynamic) suggest that CV spontaneously adsorbs onto the nanocomposite surface. CV preferentially adsorbs on the interface between TiO₂

Fig. 15 Proposed adsorption mechanism of CV dye onto PAA@TiO₂



nanoparticles and polyacrylamide polymer. The adsorption of the molecule onto this nanocomposite material is robust, as evidenced by both the adsorption energy and the closeness to the surface. The effect of pH, FTIR, MC and MD, pH_{PZC} measurement, and selectivity revealed that electrostatic attraction was the most important contribution to cationic dye adsorption, followed by hydrogen bonding and n-π interaction. Therefore, the PAA@TiO₂ nanocomposite could be classified as an effective adsorbent for the removal of CV dye.

Author Contributions DŞA: Data curation, Methodology, Writing—original draft, Writing—review & editing. HE: Data curation, Methodology, Writing—original draft, Writing—review & editing. ZMŞ: Conceptualization, Data curation, Investigation, Methodology, Project administration, Supervision, Writing—original draft, Writing—review & editing. NEM: Data curation, Methodology, Writing—original draft, Writing—review & editing. VM: Data curation, Validation, Computations, Writing—review & editing.

Funding The present study was partly supported by Abdullah Gül University Scientific Research Projects Commission.

Data Availability Not applicable.

Declarations

Conflict of interest The authors have not disclosed any competing interests.

References

- Elgarahy AM, Elwakeel KZ, Mohammad SH, Elshoubaky GA (2021) A critical review of biosorption of dyes, heavy metals and metalloids from wastewater as an efficient and green process. *Clean Eng Technol* 4:100209. <https://doi.org/10.1016/J.CLET.2021.100209>
- Mikosch N, Becker R, Schelter L et al (2020) High resolution water scarcity analysis for cotton cultivation areas in Punjab, Pakistan. *Ecol Indic* 109:105852. <https://doi.org/10.1016/J.ECOLIND.2019.105852>
- Yao T, Qiao L, Du K (2020) High tough and highly porous graphene/carbon nanotubes hybrid beads enhanced by carbonized polyacrylonitrile for efficient dyes adsorption. *Microporous Mesoporous Mater* 292:109716. <https://doi.org/10.1016/J.MICROMESO.2019.109716>
- Samsami S, Mohamadi M, Sarrafzadeh MH et al (2020) Recent advances in the treatment of dye-containing wastewater from textile industries: overview and perspectives. *Process Saf Environ Prot* 143:138–163. <https://doi.org/10.1016/J.PSEP.2020.05.034>
- El Khomri M, El Messaoudi N, Dbik A et al (2021) Regeneration of argan nutshell and almond shell using HNO₃ for their reusability to remove cationic dye from aqueous solution. *Chem Eng Commun* 209:1304–1315. <https://doi.org/10.1080/00986445.2021.1963960>
- Güyer GT, Nadeem K, Dizge N (2016) Recycling of pad-batch washing textile wastewater through advanced oxidation processes and its reusability assessment for Turkish textile industry. *J Clean Prod* 139:488–494. <https://doi.org/10.1016/J.JCLEPRO.2016.08.009>
- Lu X, Liu L, Liu R, Chen J (2010) Textile wastewater reuse as an alternative water source for dyeing and finishing processes: a case study. *Desalination* 258:229–232. <https://doi.org/10.1016/J.DESAL.2010.04.002>

8. Pereira CP, Goldenstein JPN, Bassin JP (2022) Industrial wastewater contaminants and their hazardous impacts. *Biosorption Wastewater Contam*. <https://doi.org/10.1002/9781119737629.CH1>
9. Azari A, Noorisephr M, Dehganifard E et al (2019) Experimental design, modeling and mechanism of cationic dyes biosorption on to magnetic chitosan-lutaraldehyde composite. *Int J Biol Macromol* 131:633–645. <https://doi.org/10.1016/J.IJBIOMAC.2019.03.058>
10. Li B, Lv T, Shen Y (2022) Synthesis and characterization of dual-ion-crosslinked magnetic sodium alginate-based Fe-SA-Y@Fe₃O₄ biogel composite with ultrastrong performance for azo dye removal. *J Polym Environ* 30:2847–2861. <https://doi.org/10.1007/S10924-022-02404-6/METRICS>
11. Spoială A, Ilie CI, Dolete G et al (2022) Preparation and characterization of chitosan/TiO₂ composite membranes as adsorbent materials for water purification. *Membr* 12:804. <https://doi.org/10.3390/MEMBRANES12080804>
12. Ali H, Mansor ES, Taha GM (2022) Microfiltration and adsorptive membranes for simultaneous removal of methyl orange and methylene blue using hybrid composites. *Polym Bull* 79:7891–7908. <https://doi.org/10.1007/S00289-021-03884-7/METRICS>
13. Zhang F (2017) Grand challenges for nanoscience and nanotechnology in energy and health. *Front Chem* 5:80. <https://doi.org/10.3389/FCHEM.2017.00080/BIBTEX>
14. Arun J, Nachiappan S, Rangarajan G et al (2022) Synthesis and application of titanium dioxide photocatalysis for energy, decontamination and viral disinfection: a review. *Environ Chem Lett* 21(21):339–362. <https://doi.org/10.1007/S10311-022-01503-Z>
15. Wu S, Weng Z, Liu X et al (2014) Functionalized TiO₂ based nanomaterials for biomedical applications. *Adv Funct Mater* 24:5464–5481. <https://doi.org/10.1002/ADFM.201400706>
16. Xia ZY, Yan LX, Tian C, Xi WJ (2020) Production of carbon-doped titanium dioxide (C–TiO₂) from polytitanium-coagulated sludge as an adsorbent or photocatalyst for pollutant removals. *J Clean Prod* 267:121979. <https://doi.org/10.1016/J.JCLEPRO.2020.121979>
17. Dahl M, Liu Y, Yin Y (2014) Composite titanium dioxide nanomaterials. *Chem Rev* 114:9853–9889. https://doi.org/10.1021/CR400634P/ASSET/IMAGES/LARGE/CR-2013-00634P_0035.JPEG
18. Sharma M, Behl K, Nigam S, Joshi M (2018) TiO₂-GO nanocomposite for photocatalysis and environmental applications: a green synthesis approach. *Vacuum* 156:434–439. <https://doi.org/10.1016/J.VACUUM.2018.08.009>
19. Han C, Lalley J, Namboodiri D et al (2016) Titanium dioxide-based antibacterial surfaces for water treatment. *Curr Opin Chem Eng* 11:46–51. <https://doi.org/10.1016/J.COCHE.2015.11.007>
20. MiariAlipour S, Friedmann D, Scott J, Amal R (2018) TiO₂/porous adsorbents: recent advances and novel applications. *J Hazard Mater* 341:404–423. <https://doi.org/10.1016/J.JHAZMAT.2017.07.070>
21. Utami FD, RahmanSutisna DY et al (2019) Photocatalyst based on TiO₂ and its application in organic wastewater treatment using simple spray method. *J Phys Conf Ser* 1204:012086. <https://doi.org/10.1088/1742-6596/1204/1/012086>
22. Baig U, Uddin MK, Sajid M (2020) Surface modification of TiO₂ nanoparticles using conducting polymer coating: spectroscopic, structural, morphological characterization and interaction with dye molecules. *Mater Today Commun* 25:101534. <https://doi.org/10.1016/J.MTCOMM.2020.101534>
23. Araoyinbo AO, Abdullah MMAB, Rahmat A et al (2018) Preparation of heat treated titanium dioxide (TiO₂) nanoparticles for water purification. *IOP Conf Ser Mater Sci Eng* 374:012084. <https://doi.org/10.1088/1757-899X/374/1/012084>
24. Penboon L, Khruetakham A, Sairiam S (2019) TiO₂ coated on PVDF membrane for dye wastewater treatment by a photocatalytic membrane. *Water Sci Technol* 79:958–966. <https://doi.org/10.2166/WST.2019.023>
25. Nakayama N, Hayashi T (2007) Preparation and characterization of TiO₂ and polymer nanocomposite films with high refractive index. *J Appl Polym Sci* 105:3662–3672. <https://doi.org/10.1002/APP.26451>
26. Abdelnasser S, Al Sakkaf R, Palmisano G (2021) Environmental and energy applications of TiO₂ photoanodes modified with alkali metals and polymers. *J Environ Chem Eng* 9:104873. <https://doi.org/10.1016/J.JECE.2020.104873>
27. Sun L, Guan J, Xu Q et al (2018) Synthesis and applications of molecularly imprinted polymers modified TiO₂ nanomaterials: a review. *Polym* 10:1248. <https://doi.org/10.3390/POLYM1011248>
28. El Messaoudi N, El Mouden A, Fernine Y et al (2022) Green synthesis of Ag₂O nanoparticles using Punica granatum leaf extract for sulfamethoxazole antibiotic adsorption: characterization, experimental study, modeling, and DFT calculation. *Environ Sci Pollut Res* 2022:1–18. <https://doi.org/10.1007/S11356-022-21554-7>
29. Sultan M, Nagieb ZA, El-Masry HM, Taha GM (2022) Physically-crosslinked hydroxyethyl cellulose-g-poly (acrylic acid-co-acrylamide)-Fe³⁺/silver nanoparticles for water disinfection and enhanced adsorption of basic methylene blue dye. *Int J Biol Macromol* 196:180–193. <https://doi.org/10.1016/J.IJBIOMAC.2021.11.109>
30. Lebkiri I, Abbou B, Hsissou R et al (2023) Investigation of the anionic polyacrylamide as a potential adsorbent of crystal violet dye from aqueous solution: equilibrium, kinetic, thermodynamic, DFT, MC and MD approaches. *J Mol Liq* 372:121220. <https://doi.org/10.1016/J.MOLLIQ.2023.121220>
31. Babas H, Khachani M, Warad I et al (2022) Sofosbuvir adsorption onto activated development of Arabic gum carbon derived from argan shell residue: optimization, kinetic, thermodynamic and theoretical approaches. *J Mol Liq* 356:119019. <https://doi.org/10.1016/J.MOLLIQ.2022.119019>
32. Amrhar O, Berisha A, El Gana L et al (2021) Removal of methylene blue dye by adsorption onto natural muscovite clay: experimental, theoretical and computational investigation. *Int J Environ Anal Chem*. <https://doi.org/10.1080/03067319.2021.1897119>
33. Ajebli S, Kaichouh G, Khachani M et al (2022) The adsorption of Tenofovir in aqueous solution on activated carbon produced from maize cobs: insights from experimental, molecular dynamics simulation, and DFT calculations. *Chem Phys Lett* 801:139676. <https://doi.org/10.1016/J.CPLETT.2022.139676>
34. El Mouden A, El Messaoudi N, El Guerraf A et al (2023) Multifunctional cobalt oxide nanocomposites for efficient removal of heavy metals from aqueous solutions. *Chemosphere* 317:137922. <https://doi.org/10.1016/J.CHEMOSPHERE.2023.137922>
35. Mehmeti V, Halili J, Berisha A (2022) Which is better for Lindane pesticide adsorption, graphene or graphene oxide? An experimental and DFT study. *J Mol Liq* 347:118345. <https://doi.org/10.1016/J.MOLLIQ.2021.118345>
36. Iravani D, Esmaeili N, Berisha A et al (2023) The quaternary ammonium salts as corrosion inhibitors for X65 carbon steel under sour environment in NACE 1D182 solution: experimental and computational studies. *Colloids Surf A Physicochem Eng Asp* 656:130544. <https://doi.org/10.1016/J.COLSURFA.2022.130544>
37. Ould Abdelwedoud B, Damej M, Tassaoui K et al (2022) Inhibition effect of N-propargyl saccharin as corrosion inhibitor of C38 steel in 1 M HCl, experimental and theoretical study. *J Mol Liq* 354:118784. <https://doi.org/10.1016/J.MOLLIQ.2022.118784>
38. Ouass A, Galai M, Ouakki M et al (2021) Poly(sodium acrylate) and Poly(acrylic acid sodium) as an eco-friendly corrosion

- inhibitor of mild steel in normal hydrochloric acid: experimental, spectroscopic and theoretical approach. *J Appl Electrochem* 51:1009–1032. <https://doi.org/10.1007/S10800-021-01556-Y/METRICS>
39. Danisman M, Berisha A, Dagdag O, Oral A (2022) Surface modification of hydroxyapatite with enzyme-catalyzed reaction: computation-supported experimental studies. *Mater Chem Phys* 289:126448. <https://doi.org/10.1016/J.MATCHEMPHYS.2022.126448>
 40. Toro RG, Diab M, de Caro T et al (2020) Study of the effect of titanium dioxide hydrosol on the photocatalytic and mechanical properties of paper sheets. *Mater* 13:1326. <https://doi.org/10.3390/MA13061326>
 41. Ispirli Doğanç Y, Deveci I, Teke M, Mercimek B (2014) TiO₂ beads and TiO₂-chitosan beads for urease immobilization. *Mater Sci Eng C* 42:429–435. <https://doi.org/10.1016/J.MSEC.2014.05.058>
 42. Li W, Liang R, Hu A et al (2014) Generation of oxygen vacancies in visible light activated one-dimensional iodine TiO₂ photocatalysts. *RSC Adv* 4:36959–36966. <https://doi.org/10.1039/C4RA04768K>
 43. Ertap H, Karabulut M (2018) Structural and electrical properties of boron doped InSe single crystals. *Mater Res Express* 6:035901. <https://doi.org/10.1088/2053-1591/AAF2F6>
 44. León A, Reuquen P, Garín C et al (2017) FTIR and raman characterization of TiO₂ nanoparticles coated with polyethylene glycol as carrier for 2-methoxyestradiol. *Appl Sci* 7:49. <https://doi.org/10.3390/APP7010049>
 45. Benbow NL, Rozenberga L, McQuillan AJ et al (2021) ATR FTIR study of the interaction of TiO₂ nanoparticle films with β-Lactoglobulin and bile salts. *Langmuir* 37:13278–13290. https://doi.org/10.1021/ACS.LANGMUIR.1C01830/SUPPL_FILE/LA1C01830_SI_001.PDF
 46. Tang Q, Lin J, Wu Z et al (2007) Preparation and photocatalytic degradability of TiO₂/polyacrylamide composite. *Eur Polym J* 43:2214–2220. <https://doi.org/10.1016/J.EURPOLYMJ.2007.01.054>
 47. El Messaoudi N, El Khomri M, Chegini ZG et al (2022) Desorption of crystal violet from alkali-treated agricultural material waste: an experimental study, kinetic, equilibrium and thermodynamic modeling. *Pigment Resin Technol* 51:309–319. <https://doi.org/10.1108/PRT-02-2021-0019/FULL/XML>
 48. Kazemi F, Mohamadnia Z, Kaboudin B, Karimi Z (2016) Photodegradation of methylene blue with a titanium dioxide/polyacrylamide photocatalyst under sunlight. *J Appl Polym Sci*. <https://doi.org/10.1002/APP.43386>
 49. Cheriaa J, Khaireddine M, Rouabhia M, Bakhrouf A (2012) Removal of triphenylmethane dyes by bacterial consortium. *Sci World J*. <https://doi.org/10.1100/2012/512454>
 50. Papa G, Di Prisco G, Spini G et al (2021) Acute and chronic effects of titanium dioxide (TiO₂) PM1 on honey bee gut microbiota under laboratory conditions. *Sci Rep* 11(11):1–12. <https://doi.org/10.1038/s41598-021-85153-1>
 51. Cabaleiro D, Pastoriza-Gallego MJ, Gracia-Fernández C et al (2013) Rheological and volumetric properties of TiO₂-ethylene glycol nanofluids. *Nanoscale Res Lett* 8:1–13. <https://doi.org/10.1186/1556-276X-8-286/FIGURES/8>
 52. El Khomri M, El Messaoudi N, Dbik A et al (2022) Removal of congo red from aqueous solution in single and binary mixture systems using argan nutshell wood. *Pigment Resin Technol* 51:477–488. <https://doi.org/10.1108/PRT-04-2021-0045/FULL/XML>
 53. Saad M, Tahir H, Ali D (2017) Green synthesis of Ag–Cr–AC nanocomposites by *azadirachta indica* and its application for the simultaneous removal of binary mixture of dyes by ultrasonicated assisted adsorption process using response surface methodology. *Ultrason Sonochem* 38:197–213. <https://doi.org/10.1016/J.ULTSONCH.2017.03.022>
 54. Hassan W, Farooq U, Ahmad M et al (2017) Potential biosorbent, haloxylon recurvum plant stems, for the removal of methylene blue dye. *Arab J Chem* 10:S1512–S1522. <https://doi.org/10.1016/J.ARABJC.2013.05.002>
 55. Ullatli SG, Ramakrishnan RM (2018) Defect-rich brown TiO₂-x porous flower aggregates: selective photocatalytic reversibility for organic dye degradation. *ACS Appl Nano Mater* 1:4045–4052. https://doi.org/10.1021/ACSANM.8B00824/SUPPL_FILE/AN8B00824_SI_001.PDF
 56. Jeon M, Jun BM, Kim S et al (2020) A review on MXene-based nanomaterials as adsorbents in aqueous solution. *Chemosphere* 261:127781. <https://doi.org/10.1016/J.CHEMOSPHERE.2020.127781>
 57. Shoukat S, Bhatti HN, Iqbal M, Noreen S (2017) Mango stone biocomposite preparation and application for crystal violet adsorption: a mechanistic study. *Microporous Mesoporous Mater* 239:180–189. <https://doi.org/10.1016/J.MICROMESO.2016.10.004>
 58. Özcan A, Öncü EM, Özcan AS (2006) Kinetics, isotherm and thermodynamic studies of adsorption of acid blue 193 from aqueous solutions onto natural sepiolite. *Colloids Surf A Physicochem Eng Asp* 277:90–97. <https://doi.org/10.1016/J.COLSURF.A.2005.11.017>
 59. Chakraborty S, Chowdhury S, Das Saha P (2011) Adsorption of crystal violet from aqueous solution onto NaOH-modified rice husk. *Carbohydr Polym* 86:1533–1541. <https://doi.org/10.1016/J.CARBPOL.2011.06.058>
 60. Nandi BK, Goswami A, Das AK et al (2008) Kinetic and equilibrium studies on the adsorption of crystal violet dye using kaolin as an adsorbent. *Sep Sci Technol* 43:1382–1403. <https://doi.org/10.1080/01496390701885331>
 61. Laskar N, Kumar U (2018) Adsorption of crystal violet from wastewater by modified bambusa tulda. *KSCE J Civ Eng* 22:2755–2763. <https://doi.org/10.1007/S12205-017-0473-5/METRICS>
 62. Salehi I, Shirani M, Semnani A et al (2016) Comparative study between response surface methodology and artificial neural network for adsorption of crystal violet on magnetic activated carbon. *Arab J Sci Eng* 41:2611–2621. <https://doi.org/10.1007/S13369-016-2109-3/METRICS>
 63. Khan TA, Khan EA, Shahjahan (2015) Removal of basic dyes from aqueous solution by adsorption onto binary iron-manganese oxide coated kaolinite: non-linear isotherm and kinetics modeling. *Appl Clay Sci* 107:70–77. <https://doi.org/10.1016/J.CLAY.2015.01.005>
 64. Sulyman M, Kucinska-Lipka J, Sienkiewicz M, Gierak A (2021) Development, characterization and evaluation of composite adsorbent for the adsorption of crystal violet from aqueous solution: Isotherm, kinetics, and thermodynamic studies. *Arab J Chem* 14:103115. <https://doi.org/10.1016/J.ARABJC.2021.103115>
 65. Gopi S, Pius A, Thomas S (2016) Enhanced adsorption of crystal violet by synthesized and characterized chitin nano whiskers from shrimp shell. *J Water Process Eng* 14:1–8. <https://doi.org/10.1016/J.JWPE.2016.07.010>
 66. Ahmad R (2009) Studies on adsorption of crystal violet dye from aqueous solution onto coniferous pinus bark powder (CPBP). *J Hazard Mater* 171:767–773. <https://doi.org/10.1016/J.JHAZMAT.2009.06.060>
 67. Gholami M, Vardini MT, Mahdavinia GR (2016) Investigation of the effect of magnetic particles on the crystal violet adsorption onto a novel nanocomposite based on κ-carrageenan-g-poly(methacrylic acid). *Carbohydr Polym* 136:772–781. <https://doi.org/10.1016/J.CARBPOL.2015.09.044>

68. Hamidzadeh S, Torabbeigi M, Shahtaheri SJ (2015) Removal of crystal violet from water by magnetically modified activated carbon and nanomagnetic iron oxide. *J Environ Heal Sci Eng* 13:1–7. <https://doi.org/10.1186/S40201-015-0156-4/TABLES/4>
69. Batool S, Idrees M, Ahmad M et al (2020) Design and characterization of a biomass template/SnO₂ nanocomposite for enhanced adsorption of 2,4-dichlorophenol. *Environ Res* 181:108955. <https://doi.org/10.1016/J.ENVRES.2019.108955>
70. Van TT, Nguyen DTC, Le HTN et al (2020) Optimization, equilibrium, adsorption behavior and role of surface functional groups on graphene oxide-based nanocomposite towards diclofenac drug. *J Environ Sci* 93:137–150. <https://doi.org/10.1016/J.JES.2020.02.007>
71. Ho YS, McKay G (1998) Kinetic models for the sorption of dye from aqueous solution by wood. *Process Saf Environ Prot* 76:183–191. <https://doi.org/10.1205/095758298529326>
72. Ho YS, McKay G (1999) Pseudo-second order model for sorption processes. *Process Biochem* 34:451–465. [https://doi.org/10.1016/S0032-9592\(98\)00112-5](https://doi.org/10.1016/S0032-9592(98)00112-5)
73. Weber Jr WJ, Morris JC (1963) Kinetics of Adsorption on Carbon from Solution. *J Sanit Eng Div* 89:31–59. <https://doi.org/10.1061/JSEDAI.0000430>
74. Taha GM, Mansor ES, Sultan M (2021) Development of Arabic gum-based AgTiO₂ nanocomposite hydrogel as high efficient adsorbent of cationic dye methylene blue from water. *Int J Biol Macromol* 193:1859–1870. <https://doi.org/10.1016/J.IJBIOMAC.2021.11.018>
75. Sultan M, Mansor ES, Nagieb ZA, Elsayed H (2021) Fabrication of highly efficient nano-composite films based on ZnO-g-C₃N₄@PAA-g-(HEC/PVA)-Fe³⁺ for removal of methylene blue dye from water. *J Water Process Eng* 42:102184. <https://doi.org/10.1016/J.JWPE.2021.102184>
76. El MN, El KM, Chegini ZG et al (2021) Desorption study and reusability of raw and H₂SO₄ modified jujube shells (*Zizyphus lotus*) for the methylene blue adsorption. *Int J Environ Anal Chem*. <https://doi.org/10.1080/03067319.2021.1912338>
77. Raghav S, Kumar D (2018) Adsorption equilibrium, kinetics, and thermodynamic studies of fluoride adsorbed by tetrametallic oxide adsorbent. *J Chem Eng Data* 63:1682–1697. https://doi.org/10.1021/ACS.JCED.8B00024/SUPPL_FILE/IE8B00024_SI_001.PDF
78. El Messaoudi N, El MA, El KM et al (2022) Experimental study and theoretical statistical modeling of acid blue 25 remediation using activated carbon from *Citrus sinensis* leaf. *Fluid Phase Equilib* 563:113585. <https://doi.org/10.1016/J.FLUID.2022.113585>
79. Al-Ajji MA, Al-Ghouthi MA (2021) Novel insights into the nano-adsorption mechanisms of crystal violet using nano-hazelnut shell from aqueous solution. *J Water Process Eng* 44:102354. <https://doi.org/10.1016/J.JWPE.2021.102354>
80. Guo L, Zhang ST, Li WP et al (2014) Experimental and computational studies of two antibacterial drugs as corrosion inhibitors for mild steel in acid media. *Mater Corros* 65:935–942. <https://doi.org/10.1002/maco.201307346>
81. Hsissou R, Dagdag O, About S et al (2019) Novel derivative epoxy resin TGETET as a corrosion inhibition of E24 carbon steel in 1.0 M HCl solution. Experimental and computational (DFT and MD simulations) methods. *J Mol Liq* 284:182–192. <https://doi.org/10.1016/J.MOLLIQ.2019.03.180>
82. Dagdag O, Hsissou R, El Harfi A et al (2020) Fabrication of polymer based epoxy resin as effective anti-corrosive coating for steel: computational modeling reinforced experimental studies. *Surf Interfaces* 18:100454. <https://doi.org/10.1016/j.surfin.2020.100454>
83. Dagdag O, Safi Z, Hamed O et al (2021) Comparative study of some epoxy polymers based on bisphenolic and aromatic diamines: synthesis, viscosity, thermal properties computational and statistical approaches. *J Polym Res* 285(28):1–16. <https://doi.org/10.1007/S10965-021-02530-0>
84. Nairat N, Hamed O, Berisha A et al (2022) Cellulose polymers with β -amino ester pendant group: design, synthesis, molecular docking and application in adsorption of toxic metals from wastewater. *BMC Chem* 16(16):1–21. <https://doi.org/10.1186/S13065-022-00837-7>
85. Jafari H, Ameri E, Rezaeivala M, Berisha A (2022) 4,4'-(((2,2-Dimethylpropane-1,3-Diyl)Bis(Azanediy1)Bis(Methylene)Bis(2-Methoxyphenol) as new reduced form of schiff base for protecting API 5L grade B in 1 M HCl. *Arab J Sci Eng*. <https://doi.org/10.1007/S13369-022-07281-8/METRICS>
86. Jafari H, Ameri E, Rezaeivala M et al (2022) Anti-corrosion behavior of two N₂O₄ Schiff-base ligands: experimental and theoretical studies. *J Phys Chem Solids* 164:110645. <https://doi.org/10.1016/J.JPCS.2022.110645>
87. Dagdag O, Berisha A, Mehmeti V et al (2022) Epoxy coating as effective anti-corrosive polymeric material for aluminum alloys: formulation, electrochemical and computational approaches. *J Mol Liq* 346:117886. <https://doi.org/10.1016/J.MOLLIQ.2021.117886>
88. Rahimi A, Farhadian A, Berisha A et al (2022) Novel sucrose derivative as a thermally stable inhibitor for mild steel corrosion in 15% HCl medium: an experimental and computational study. *Chem Eng J* 446:136938. <https://doi.org/10.1016/J.CEJ.2022.136938>

Publisher's Note Springer Nature remains neutral with regard to jurisdictional claims in published maps and institutional affiliations.

Springer Nature or its licensor (e.g. a society or other partner) holds exclusive rights to this article under a publishing agreement with the author(s) or other rightsholder(s); author self-archiving of the accepted manuscript version of this article is solely governed by the terms of such publishing agreement and applicable law.